# Texture evolution of sheared liquid crystalline polymers: Numerical predictions of roll-cells instability, director turbulence, and striped texture with a molecular model

Giorgia Sgalari and L. Gary Leal[a]

*Department of Chemical Engineering, University of California at Santa Barbara, Santa Barbara, California 93106-5080*

Eckart Meiburg

*Department of Mechanical and Environmental Engineering, University of California at Santa Barbara, Santa Barbara, California 93106-5080*

### Synopsis

In the present work, we study the textural evolution of liquid crystal polymer (LCP) systems under planar shear at high shear rates, based on computational simulations using a recently developed molecular model with distortional elasticity [Feng *et al.* (2000)]. We concentrate our attention on the final striped texture that is observed in real LCP systems and on the secondary flow instability characterized by the formation of cross-sectional roll cells that is believed to represent the starting point of the orientational evolution. We verify that the theoretical model is capable of predicting a texture evolution that captures many of the essential features of the interplay between shear flow and LCP microstructure that are observed in experiments. We identify the mechanisms at play and the relative roles of the various forces in determining the evolution of texture at moderate shear rates and how they depend on the Deborah number, which is the characteristic parameter that defines the different regimes at moderate and high values of shear rate. © *2003 The Society of Rheology.* [DOI: 10.1122/1.1621420]

## I. INTRODUCTION

### A. Motivations and summary

There has been a long history of scientific interest in liquid crystalline polymers (LCPs), but relatively few technological applications other than the production of high tensile strength fibers because of the intrinsic difficulty of maintaining a monodomain orientational state at the macroscopic level, or at least of controlling the microstructural orientation state in any processing flow other than fiber spinning.

When a nematic LCP undergoes a processing flow that involves a component of shear (e.g., flow into a mold), there is an immediate formation and/or proliferation of singular structures (points or lines) in the orientation field—known as disclinations—that are highly detrimental to the properties of the resulting product. Since this does not occur in the extensional motion of fiber spinning, we may conclude that the nature of the flow is

---

[a]Author to whom correspondence should be addressed; electronic mail: lgl20@engineering.ucsb.edu

an important factor in determining the material microstructure. Moreover, experimental observations [e.g., Mather *et al.* (1996)] have shown that disclinations are much less common in small-molecule nematics, which in general adopt a fixed orientation near the flow direction when subject to shear flow. In polymeric LCs, on the other hand, the average direction of orientation almost always rotates continuously in a shearing flow (they exhibit "tumbling" behavior). It is generally believed that this difference in the tumbling versus flow-aligning response when subjected to shear is crucial for the appearance of the cascade of flow instabilities that one observes in LCP materials. However, a detailed understanding of the physical mechanisms that determine the evolution of texture and its interaction with the flow, which is of crucial importance to any future development of processing protocols for LCPs as structural materials, is still missing.

The main goal of the present work has been to develop a theoretical model and numerical tools that will capture the essential features of the textural evolution in shear flow at moderate to high shear rates (i.e., the so-called Deborah number cascade that will be discussed in more detail in the following section). In the process, we hope to better understand the roles of the various mechanisms in this textural evolution process and thus provide a basic platform toward the prediction of LCP material response to processing flows which are generally characterized by these high values of shear rates (as well as the possibility of tailoring these flows to better control material structure).

A series of previous theoretical works [extended most recently by the work of Feng *et al.* (2001)] have utilized the Leslie–Ericksen (LE) theory to explore the different types of texture evolution that occur at lower values of the shear rates (i.e., the so-called Ericksen number cascade). These works, however, cannot be extended to the analysis of the Deborah number cascade since, in this regime, one cannot neglect the effects of molecular viscoelasticity (which is not accounted for in the LE model). These works cannot capture therefore some of the phenomena that characterize this regime, such as the strong reduction of orientational order that occurs at each material point as the shear rate is increased or the formation of the so-called "thin" disclinations with isotropic cores. As indicated earlier, this paper generalizes the preceding analysis to include high Deborah number flows.

The paper is organized as follows. We will briefly summarize the existing body of experimental observations and previous numerical works. We will then describe the setup of our problem, review the main features of the theoretical model used, and highlight the most important aspects of the numerical scheme developed for this problem. We then present results obtained for the subset of the parameter space, corresponding to moderate-high values of the Deborah number, showing detailed predictions of the evolution of texture and how the evolution changes with the Deborah number in the range of shear rates examined. The main features of the roll-cell instability and of the ensuing striated texture, that our simulations are able to predict, will then be compared with several of the existing experimental observations [Larson and Mead (1993), Tan and Berry (2003)] and with the physical picture proposed by Feng *et al.* (2001) for the LE fluid.

## B. Experimental observations

A number of experimental observations have characterized the optical, rheological and scattering properties of various LCP solutions undergoing planar shear (e.g., Larson and Mead (1992, 1993) on PBG solution, Vermant *et al.* (1994) on HPC, and Tan and Berry (2003) on PBT, Walker *et al.* (2000)]. From this body of work, a relatively detailed picture of the macroscopic signatures of the textural evolution of these materials is now available. We summarize the microstructural/rheological behavior and its dependence on shear rate based upon the seminal papers by Larson and Mead (1992, 1993), which

present optical observations of the textural evolution of a typical LCP solution (PBG) during planar steady shear flow.

The Ericksen (Er) number (i.e., the ratio between the strength of distortional elasticity and viscous effects) is the characteristic parameter that determines the type of transitions observed in sheared liquid crystalline polymers at "low" shear rates [i.e., shear rates such that the Deborah number remains O(1) or smaller, even as Er may become quite large]. These different transitions constitute what has come to be known as the *Ericksen number cascade*. Specifically, for very low values of the Ericksen number, the director first rotates towards the vorticity direction, followed by the appearance of roll cells and birefringent stripes both oriented in the flow direction. This roll-cell structure becomes progressively fine scale with further increase of the Ericksen number, with a decrease of roll spacing that scales between the power laws $Er^{-1/4}$ and $Er^{-1/2}$. For even larger Ericksen numbers, the observed striped pattern becomes too irregular for a single dominant stripe width to be derived from experimental observations. For these values of the Ericksen numbers, $Er \sim 10^4 - 10^6$, the director field is spatially irregular and time dependent with disclination lines generated in abundance and the system is said to exhibit director turbulence [Manneville (1981)]. The changes in the structure of the flow with increasing Er number are similar in some respects to the changes in the structure of the Taylor-vortex flow between concentric cylinders as the Reynolds number is increased [Lathrop *et al.* (1992)]. The refinement of the texture that occurs at high Er number is characterized by large viscous stresses which act on domains that become smaller and smaller as the shear rate is increased. Eventually, the shear rate is high enough for individual molecules to experience significant viscous torques, allowing the molecular order parameter to be distorted from its equilibrium value. This occurs when the Deborah number (i.e., the ratio between the strength of molecular elasticity and viscous effects) approaches or exceeds unity. At these high shear rates, the system is said to have entered the *Deborah number cascade*. In this regime, it is the Deborah (De) number, and not the Ericksen number, that controls the further evolution of the texture.

Specifically, for values of De number above 1 but below the tumbling-wagging transition, a very fine worm texture is observed. This regime is still characterized by a state of director turbulence with the microstructural length scale decreasing as the shear rate is increased. Since the director turbulence disrupts the average orientation of the sample, the birefringence of samples in the tumbling regime is significantly less than that of a monodomain. For higher shear rates, i.e., for values of the De number in the so-called wagging regime, a distinct striped texture reappears. This texture is characterized by relatively wide stripes whose characteristic width is only weakly dependent on shear rate [Gleeson *et al.* (1992), Larson and Mead (1992)]. It is still unclear whether this reappearance of a striped texture is due to the same type of physical mechanism that leads to the roll cell instability at low Er number (e.g., Vermant *et al.* (1994)] and/or it is due to enhanced fluctuations near the wagging transition [Larson and Mead (1993)]. The regularity and the definition of the stripes progressively decreases with increasing shear rate [Tan and Berry (2003)], until, finally, at shear rates corresponding to values of Deborah number in the flow-aligning regime, a uniform monodomain develops.

Figure 1 summarizes the earlier described transitions of the Ericksen and Deborah number cascades. The areas of parameter space covered by the Larson and Mead paper are indicated by thick lines, while the cases examined in the current work are indicated by diamonds.

As a final remark, we note that, according to some of the indicated observations, the evolution of a real LCP system undergoing shear flow starting from a parallel or homeotropic monodomain, is initially characterized by the appearance of a transient banded
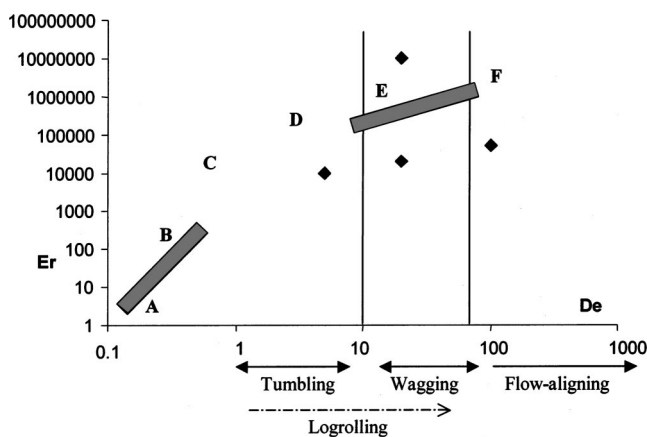
**FIG. 1.** Summary of Larson and Mead (1993) experimental observations: Ericksen number cascade (A–C) and Deborah number cascade (D–F). A. Stable system, B. roll cell instability and striped texture, C. director turbulence, D. fine worm texture, E. roll-cell instability and well defined striped texture, and F. flow-aligned monodomain. The bars indicate the regions in which a striped pattern was observed. The diamonds indicate the case that we studied in the present work.

texture perpendicular to the flow direction. In a recent paper [Sgalari *et al.* (2002)], we utilized the same Doi–Marrucci model used here along with a numerical procedure that allowed gradients only in the velocity–velocity gradient plane to analyze the banded structure and some of its features. In the present work, we allow gradients only in the vorticity-velocity gradient direction and not in the flow direction. Hence, we are not able to predict the initial banded structure, but we can predict the streamwise roll cell structure that was not possible in the previous study.

## C. Background of numerical simulations

A number of prior numerical investigations of LC flow have been done using the LE model. The study that is most closely related to the present work is the recent paper of Feng *et al.* (2001). These authors considered a simple shear flow with a fully three-dimensional (3D) orientational space for the director but with spatial gradients limited to the velocity-gradient vorticity plane. In this framework, they were able to capture the onset of a secondary flow instability at low values of the shear rate (and low values of the Ericksen number) with the prediction of roll cells oriented in the flow direction. The most important result of these simulations was that a detailed mechanism was found for the formation of coreless (i.e., "thick") disclinations. However, these defect lines appeared at the center of the original roll cells, while it seems to be commonly accepted in the LCP literature that disclinations should form between the cells predominantly. Indeed, the only direct experimental observations that we are aware of (for small molecule LCs) point to a larger concentration of disclinations at the cell boundaries for low values of the Er number rather than at the center of the rolls [Mather *et al.* (1996)]. However, we were unable to find any detailed analysis of the disclinations that appear in LCPs, and it is quite possible that the disclinations that (apparently) appear between the roll cells in these systems are of the "thin" type with a defect core of significantly reduced order [Marrucci and Greco (1994)]. Since the simulations of Feng *et al.* were done using the LE theory, the presence of such thin disclinations could not be captured. In fact, the LE model leaves out, as already noted, the potentially critical viscoelastic effects due to distortions of the orientation distribution, which are an essential characteristic of the textural evolution of
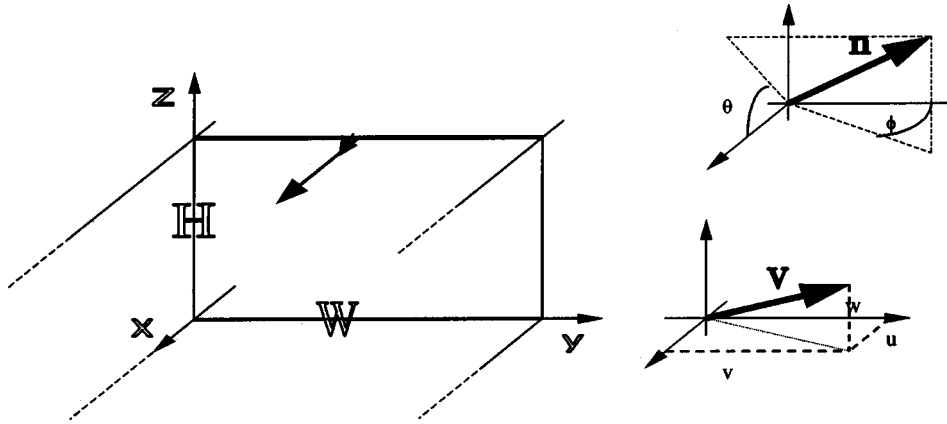
**FIG. 2.** System geometry (indicated in blue the velocity imposed on the upper wall), components of the velocity **v** and angles that define the director **n**.

LCP systems at the higher shear rates (i.e., higher Er number) characteristic of both processing flows and the existing experimental observations.

Prior to the present study, a series of works had tried to overcome these limitations of the LE model for the study of textural evolution of LCPs at moderate to high shear rates. However, these were all based on the so-called monodomain Doi theory [Feng and Leal (1999); Feng *et al.* (1998)], which correctly accounts for the effects of viscoelasticity, but does not include gradient (i.e., distortional) elasticity. These works showed that the Doi theory predicts the formation of disclinations when there are spatial gradients in the rate of director tumbling due to spatial variations of the shear rate. No disclinations are possible in homogeneous (simple) shear flow because the anchoring of orientation at the boundaries is not taken into account. Moreover, in the absence of distortional elasticity, the disclinations are only transient structures that are continuously annihilated and re-formed, rather than reaching a final "steady-state" structure as is generally believed to occur in the real system [Marrucci and Greco (1994)].

A very recent numerical work [Kupfermann *et al.* (2000)] tried then to incorporate the effect of distortional elasticity into the original Doi formulation. Even though this work was the first with full coupling between flow and microstructural evolution, its relevance is limited because of the restrictions of the numerical approximation (one-dimensional flow-two-dimensional orientation) that they analyzed.

## II. PROBLEM FORMULATION

### A. Geometry of the system

We study the evolution of a 3D shear flow driven in a shear cell by motion of the upper boundary with velocity $V$. Following the approach of Feng *et al.*, we study the problem in the plane formed by the vorticity and velocity gradient directions. As shown in Fig. 2, our computational domain is a cross section of gap height $H$ and width $W$. This simplification of the full 3D geometry retains the spatial coordinates that are essential to predict the secondary flow instability, i.e., the vorticity and shear gradient directions. Specifically, while the velocity and orientation fields are both fully three dimensional we neglect any dependence of the earlier-mentioned variables along the flow direction. Thus, there are three nonzero components $(u,v,w)$ of the velocity **v**, as shown in Fig. 2, and five independent components of the configuration tensor, but we assume that these vari-

ables depend only on the two spatial coordinates $y$ and $z$, with $y$ being the vorticity direction and $z$ the velocity gradient direction. In Fig. 2 we also define the angles that will be used to specify the orientation of the director $\mathbf{n}$ (i.e., the main eigenvector of the so-called configuration tensor $\mathbf{S}$ that will be defined later).

## B. Model equations

The kinetic equation governing the evolution of the LCP configuration, and the corresponding expression for the stress tensor are those of the Doi/Marrucci model, as developed in Feng $et\ al.$ (2000). The model is a molecularly-based constitutive theory for nematic LCPs that incorporates distortional elasticity via the Marrucci–Greco potential [Marrucci and Greco (1991 1994)], which is a nonlocal mean-field nematic potential for LCPs that accounts for distortional elasticity caused by spatial variations of the molecular orientation.

As in all molecular theories of LCPs, the orientational state of the material is described by a configuration tensor $\mathbf{S}$, which is the second moment of the distribution function of the molecular orientation $\mathbf{u}$. The evolution equation for $\mathbf{S}$ reads

$$\frac{D\mathbf{S}}{Dt} - (\boldsymbol{\nabla}\mathbf{v})^T \cdot \mathbf{S} - \mathbf{S} \cdot (\boldsymbol{\nabla}\mathbf{v})^T = -2(\boldsymbol{\nabla}\mathbf{v})^T : \langle \mathbf{uuuu} \rangle - \frac{f}{\text{De}}\left(\mathbf{S} - \frac{\mathbf{I}}{3}\right) + \frac{Uf}{\text{De}}(\mathbf{S}\cdot\mathbf{S} - \mathbf{S}:\langle \mathbf{uuuu} \rangle)$$

$$+ \frac{Uf}{48\text{De}}\left(\frac{\lambda}{H}\right)^2 (\boldsymbol{\nabla}^2\mathbf{S}\cdot\mathbf{S} + \mathbf{S}\cdot\boldsymbol{\nabla}^2\mathbf{S} - 2\boldsymbol{\nabla}^2\mathbf{S}:\langle \mathbf{uuuu} \rangle). \qquad (1)$$

In the earlier expression $\mathbf{v}$ is the velocity and the parameter $\lambda$ is the characteristic length scale of the Marrucci–Greco potential

$$U_{\text{MG}}(\mathbf{u}) = -\frac{3}{2}kTU\left(\mathbf{S} + \frac{\lambda^2}{24}\boldsymbol{\nabla}^2\mathbf{S}\right):\mathbf{uu},$$

which adds a nonlocal distortional elasticity to the classic Maier–Saupe potential for local nematic effects. Here $U$ is the strength of the nematic potential, $k$ is the Boltzmann constant, $T$ is the absolute temperature. The function $f$ accounts for the dependence of the rotational diffusivity on the local degree of order and is given in the form

$$f = \frac{\bar{D}_r}{D_{r0}} = \frac{D_{r0}}{\beta}\frac{1}{(1 - \mathbf{S}:\mathbf{S})^2}$$

with $\beta$ the so-called crowdedness parameter, $\bar{D}_r$ is the angular average of the rotational diffusivity of the nematic phase, and $D_{r0}$ is the rotational diffusivity in the isotropic phase. De is the Deborah number, one of the two dimensionless characteristic parameters of the system. It is defined as

$$\text{De} = \frac{V/H}{(6\bar{D}_{r0})},$$

where, again, the velocity of the upper boundary is $V$ and the gap height is $H$. The other characteristic number is the Ericksen number, Er, that is defined as

$$\text{Er} = \left(\frac{H}{\lambda}\right)^2\frac{\text{De}}{U}.$$

Finally, coupled to the evolution of the orientation field one has the momentum and continuity equations. We choose to formulate these equations in terms of the vorticity rather than the usual pressure-velocity formulation. We shall see that this allows us to use a single grid for all system variables. Due the complexity of the equations involved, this advantage in terms of program ''slimness'' is particularly relevant. Moreover, the evolution of the resulting flow field (i.e., the appearance of roll cells) is best analyzed in terms of the streamwise vorticity component, $\omega_x$.

In the vorticity formulation, the flow equations read

$$\nabla^2 \boldsymbol{\omega} = -\nabla \times (\nabla \cdot \boldsymbol{\sigma}), \tag{2}$$

$$\nabla^2 \mathbf{v} = -\nabla \times \boldsymbol{\omega}, \tag{3}$$

where $\mathbf{v}$ is the velocity field and $\boldsymbol{\omega}$ is the vorticity

$$\boldsymbol{\omega} = \nabla \times \mathbf{v}. \tag{4}$$

The stress tensor $\boldsymbol{\sigma}$ for the liquid crystalline polymer is related to the statistical configuration tensors $\mathbf{S}$ and $\langle \mathbf{uuuu} \rangle$ via the expression, first derived by Feng *et al.* (2000):

$$\boldsymbol{\sigma} = 3c \left[ \mathbf{S} - U(\mathbf{S} \cdot \mathbf{S} - \mathbf{S} : \langle \mathbf{uuuu} \rangle) - \frac{U\lambda^2}{24} \left( \mathbf{S} \cdot \nabla^2 \mathbf{S} - \langle \mathbf{uuuu} \rangle : \nabla^2 \mathbf{S} + \frac{\nabla \mathbf{S} : \nabla \mathbf{S} - \nabla \nabla \mathbf{S} : \mathbf{S}}{4} \right) \right]$$

$$+ \frac{c}{2} (\nabla \mathbf{v})^T : \langle \mathbf{uuuu} \rangle, \tag{5}$$

where $c$ is the so-called coupling parameter. It is evident that the model Eqs. (1) and (5) involve not only the second moment tensor $\mathbf{S}$, but also the fourth moment $\langle \mathbf{uuuu} \rangle$. In order to complete the specification of the problem, we require a closure approximation to relate the fourth moment to the second. As discussed in our previous paper [Sgalari *et al.* (2002)], we use a combination of the quadratic and *Bingham* closures. The Bingham closure, introduced by Chaubal and Leal (1998), is based on assuming a particular form of the angular distribution function and it is implemented via a numerical, approximate, relation between the fourth moment tensor and the second moment tensor [for a discussion of the role of different choices of closure approximations in simulating flows of LCP see, e.g., Feng *et al.* (1998), Wang and Weinan (2002), Edwards (2002)].

We note that all length scales are nondimensionalized with the characteristic gap height $H$, and time is scaled with the inverse of the characteristic shear rate imposed on the upper wall.

## C. Boundary and initial conditions

As boundary conditions, we assumed the upper and lower walls to be no-slip surfaces, i.e.:

$$u|_{z=0,1} = 0,1 \quad v|_{z=0,1} = w|_{z=0,1} = 0. \tag{6}$$

At these walls, we also required anchoring in the vorticity direction with the configuration tensor in its equilibrium form, i.e:

$$\mathbf{S}|_{z=0,1} = s_{\mathrm{eq}} \mathbf{nn}, \tag{7}$$

where $\mathbf{n} = (0,1,0)$. Here $s_{\mathrm{eq}}$ is the equilibrium value of the order parameter for a uniaxial nematic, which can be obtained from Eq. (1) using the local part of the nematic potential (i.e., the first term in the Marrucci–Greco potential).

The choice of anchoring in the vorticity direction is made for convenience. Experimental observations indicate, in fact, that when the orientation at the boundary and the initial orientation are both in the vorticity direction, the roll-cell instability is the first disturbance that drives the orientation field away from a uniform state. Thus, although roll cells develop eventually for any type of anchoring and initial orientations, the choice of anchoring in the vorticity direction makes the analysis of the roll-cell instability much simpler [Larson (1992)].

Since the characteristic width of real experimental shear cells in the vorticity direction is an order of magnitude larger than the height, a natural way to capture the essential nature of the system geometry is to assume that our computational domain is just a part of a periodic array of boxes of width $W$ in the vorticity direction. On the left and right sides, we assumed therefore periodic boundary conditions for the configuration tensor, i.e.:

$$\mathbf{S}|_{y=0} = \mathbf{S}|_{y=W/H}, \quad \frac{\partial \mathbf{S}}{\partial y}\bigg|_{y=0} = \frac{\partial \mathbf{S}}{\partial y}\bigg|_{y=W/H}. \tag{8}$$

Following Larson (1992) and Feng *et al.* (2001), the velocity field at $y = 0, W/H$ was assumed to be of the form

$$v = 0, \quad \frac{\partial u}{\partial y} = \frac{\partial w}{\partial y} = 0. \tag{9}$$

These boundary conditions correspond to the so-called slippery sides. As in Feng *et al.* (2001), fully periodic boundary conditions for the velocity field were not used since they introduce an artificial cross-flow instability. Apparently, impermeable side walls are necessary to avoid this effect (impermeable side walls are, of course, also present in the experiments).

As initial conditions, we assumed a uniform orientation along the vorticity direction as defined by the anchoring conditions Eq. (5) and a (fully developed) linear velocity profile as imposed by the velocity applied on the upper wall, i.e.:

$$u|_{t=0} = z, \quad v|_{t=0} = w|_{t=0} = 0. \tag{10}$$

## III. NUMERICAL SCHEME

At every time step, the model equations are solved sequentially by a configuration solver that solves Eq. (1) and by a flow solver.

### A. Configuration solver

The numerical scheme for the solution of the configuration equation [Eq. (1)] is based on an iterative solution of the equation that is obtained by linearizing Eq. (1), i.e.:

$$\frac{\mathbf{S}^i - \mathbf{S}^0}{\Delta t} + \mathbf{v} \cdot \nabla \mathbf{S}^{i-1} - (\nabla \mathbf{v})^T \cdot \mathbf{S}^i - \mathbf{S}^i \cdot \nabla \mathbf{v}$$

$$= -2\nabla \mathbf{v} : \mathbf{Q}_{\text{bingham}}^{i-1} - \frac{f}{\text{De}}\left(\mathbf{S}^i - \frac{\mathbf{I}}{3}\right) + \frac{Uf}{\text{De}}[(-\mathbf{S}^{i-1}:\mathbf{S}^{i-1})\mathbf{S}^i + \mathbf{S}^{i-1} \cdot \mathbf{S}^{i-1}]$$

$$+ \frac{Uf}{48\text{De}}\left(\frac{\lambda}{H}\right)^2 [2(-\nabla^2\mathbf{S}^{i-1}:\mathbf{S}^{i-1})\mathbf{S}^i + \nabla^2\mathbf{S}^{i-1} \cdot \mathbf{S}^{i-1} + \mathbf{S}^{i-1} \cdot \nabla^2\mathbf{S}^{i-1}]. \tag{11}$$

The superscript indicates the iteration number at a given time step, $\mathbf{S}^0$ is the configuration tensor field at the previous time step, $\mathbf{Q}_{\text{bingham}}$ is the fourth order moment computed according to the Bingham closure approximation, and $\mathbf{v}$ is the velocity field as computed from the flow solver at the time step considered.

This iterative solution scheme is able to treat effectively the nonlinear terms as well as the second-order derivatives and the resulting mixed implicit-explicit treatment converges in a few iterations ($< 10$).

## B. Flow solver

The solution of the flow Eqs. (2)–(3) is based on the use of spectral expansion techniques. Since we are interested in solutions that are periodic along the vorticity direction, we used a spectral expansion in that direction for the solution of the flow field. To satisfy the chosen boundary conditions, we assume the flow variables, i.e., vorticity and velocity, to be of the form

$$\omega_x(y,z) = \sum_k a_k(z)\sin\left(2\pi\frac{k}{H}y\right),$$

$$\omega_y(y,z) = \sum_k b_k(z)\cos\left(2\pi\frac{k}{H}y\right), \tag{12}$$

$$\omega_z(y,z) = \sum_k c_k(z)\sin\left(2\pi\frac{k}{H}y\right),$$

$$u(y,z) = \sum_k d_k(z)\cos\left(2\pi\frac{k}{H}y\right),$$

$$v(y,z) = \sum_k e_k(z)\sin\left(2\pi\frac{k}{H}y\right), \tag{13}$$

$$w(y,z) = \sum_k f_k(z)\cos\left(2\pi\frac{k}{H}y\right).$$

These Fourier expansions include the $k$ modes up to that defined by the characteristic size of the mesh discretization (i.e., $L/\Delta y$).

The overall structure of the flow solver can be summarized as follows.

(1) The stress due to the liquid crystal is computed in real space according to Eq. (3).
(2) The stress is transformed by fast Fourier transform (FFT) and serves as input for the solution of the Fourier transform of Eq. (9) which allows us to calculate the coefficients $a,b,c$ of the vorticity field (the solution technique is described later).
(3) The coefficients $a$, $b$, $c$ serve as input for the solution of the Fourier transform of Eq. (11) which allows us to calculate the coefficients $d,e,f$ of the velocity field.
(4) The coefficients $d,e,f$ are converted back with an inverse FFT to real space, thus providing the updated velocity field as output.

The flow equations for the Fourier coefficient functions are solved using a sixth order compact finite difference scheme for the first and second derivatives in the velocity-gradient direction. This scheme is a modification of the traditional finite difference approximation of spatial derivatives that mimics the global dependence on all nodal values

that is characteristic of spectral methods [see Lele (1992) for complete discussion of the mathematical formulation and the different possible generalizations]. The computation of spatial derivatives results in the solution of linear systems with pentadiagonal system matrices, which are treated directly by the standard Thomas algorithm.

## C. Mesh and time discretization

Due to the particular nature of the system, in which spatial gradients play a critical role in determining the evolution of the textural instability, the choice of mesh size is a key issue for the present numerical work. In fact, it was necessary to compromise between the need for an accurate description of the texture evolution at a mesoscopic level and the computational cost, in terms of memory space and time. The compromise choice that we made was to use discretization grids with mesh size $\Delta y \sim 1/32$ (i.e., 256*33 nodes) in order to capture details of texture at least down to the characteristic length scale of distortional elasticity, $\lambda$, which, as will be mentioned in the next section, we fixed for most of the cases at 0.03. Quantitative convergence with mesh size (for a mesh with four times as many nodes) was verified for some of the mesoscopic quantities that characterize the roll-cell instability, i.e., the aspect ratio of the rolls and the characteristic length scale of the rolls when the breakup process starts, as well as qualitative convergence of the evolution of all fields. It is important to note that the convergence checks between the various mesh sizes were performed at corresponding stages in the textural evolution (at the onset of the instability e.g.) for each of the two mesh sizes and not at the same time. The time scales that characterize the onset and evolution of the instability are, in fact, affected by the discretization size, suggesting the possible risk of accelerating the natural evolution of the instability with numerical round-off effects. We will therefore comment in the following only about the evolution of our system without considering the absolute magnitude of the time scale of each transition.

As far as the time discretization is concerned, we tested both a fully explicit scheme (i.e., purely sequential) solution of the flow and configuration problems, as well as an implicit scheme coupling the configuration and flow solvers, with recursive solution of the configuration and flow Eqs. (11)–(13) at time $t$ until convergence of the tensor and velocity field are obtained. The results obtained by these two schemes did not differ when the simulations were performed with small enough time steps, i.e., $\Delta t < 10^{-4}$. For the implicit scheme, we also verified convergence of the resulting fields for a larger range of time steps ($10^{-5} < \Delta t < 10^{-2}$) and we saw that even for the larger time step the initial evolution is still captured with accuracy, even if the predicted structure fields differed, in certain regions, from those with smaller time steps. For such a value of time step the appearance, at later times, of quantitative discrepancies with the results of simulations for smaller time steps coincided with the nonconvergence of the recursive solver coupling the flow and configuration solvers.

The results that we will show in the following were obtained with a mesh having a characteristic size of 0.03, with an explicit scheme for time discretization and a time step of $10^{-4}$. We refer the interested reader to Sgalari (2002) for plots with different mesh and time discretizations.

## D. Choice of parameters

As mentioned in the introduction, depending on the range of shear rate (and then of the Deborah and Ericksen numbers) that one considers, the LCP behavior observed in experiments is dramatically different. The choice of this parameter is then of crucial importance in defining the problem and the relevant questions to be addressed. In the
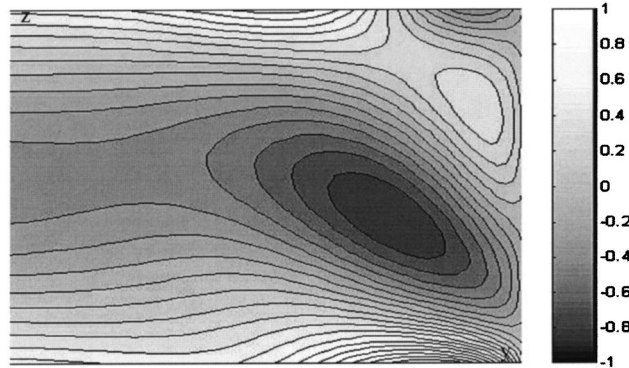
**FIG. 3.** Secondary vorticity field $\omega_x$ near the right side of the flow cell; De = 20, $t$ = 1 su: The area shown is for $y$ (6–8) and $z$ (0–1).

present work, we varied Deborah number in the range (5–100), while we kept the ratio $\lambda/H$ fixed at 0.03 for most of our calculations [the values of the Ericksen number we analyzed were then in the range $(10^3-10^4)$]. To test the qualitative behavior for larger values of the Er number, we also performed one run with $\lambda/H = 0.001$. In Fig. 1, we show the cases we have chosen to study in relation to the region of parameter space explored by the experimental observations of Larson and Mead (1993).

We used the values for $\beta$ and $c$ that were already adopted in our earlier work [Sgalari *et al.* (2002)], namely, 200 and 100, respectively. The strength of the nematic potential $U$ is fixed at 8. It is important to note that with this value of $U$, the monodomain Doi model predicts a transition from tumbling to wagging behavior at a value of De = O(10) (the exact value varies slightly depending on what closure approximation one uses), a value that is consistent with what is indicated for the PBG solutions in Larson and Mead (1993).

For the geometrical parameters of the problem (as indicated in Fig. 2), most of the calculations were performed with $W/H = 8$ since preliminary checks have assured us that increasing the aspect ratio of our shear cell beyond 8 did not qualitatively change the evolution of the results. On the other hand, reduction of the aspect ratio to smaller values was instead not tried since the computational domain would have become too small to accommodate a number of rolls sufficient for experimental comparison.

## IV. RESULTS

For all values of the Deborah number studied, our simulations showed that the LCP system in planar shear flow is unstable to the formation of secondary roll cells in the streamwise direction. In the present section, we will first discuss the typical evolution of the secondary velocity and of the orientation fields by showing the prediction of our calculations for the case of De = 20. We will then comment on quantitative and qualitative differences in the evolution of texture for the other values of the De and Er numbers that we analyzed.

### A. Roll-cell instability

The first observable effect in the evolution of our system is the generation of a recirculating pattern of secondary flow near the side edges. In Fig. 3 we show this secondary flow at a dimensionless time $t = 1$ su ("strain unit") by presenting the contour lines of the secondary vorticity $\omega_x$ near the right side of the cell. The secondary flow structure is
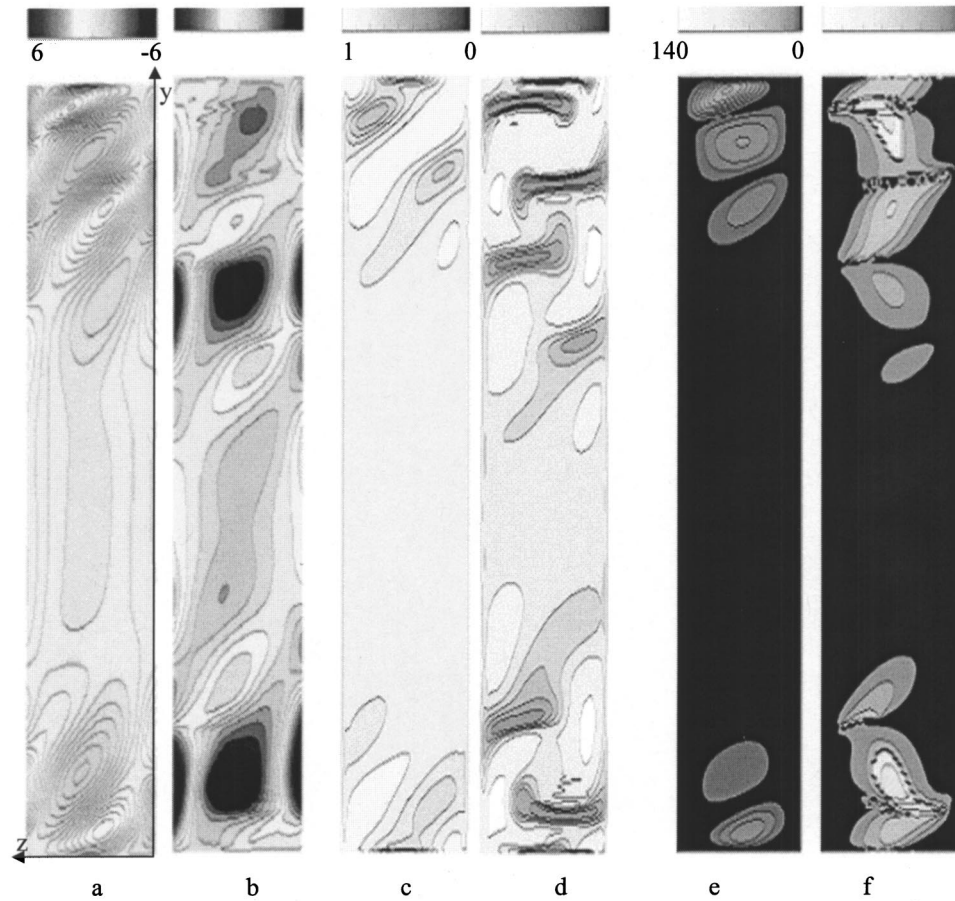
**FIG. 4.** Progressive evolution of the roll cell structure: for De = 20. (a) Secondary vorticity $\omega_x$ at $t = 1.6$ su and (b) at $t = 2.4$ su; (c) scalar order parameter field $s$ at $t = 1.6$ su and (d) at $t = 2.4$ su; director angle $\phi$ at $t = 1.6$ su and (e) at $t = 2.4$ su.

initially slightly tilted with respect to the velocity gradient direction and it is constituted by a nonsymmetric pair of counter-rotating roll cells. The roll pair spans the entire height of the gap and it is characterized by an aspect ratio of order 1. We note that this value is in agreement with the aspect ratio predicted by Feng *et al.* (2001) for the roll-cell structure in the Ericksen number cascade.

We believe that the observed strong asymmetry in the initial roll pair is not due to numerical artifacts. For example, it is completely unaffected by any reversal in the direction of computational scanning. Still unclear, however, is the physical origin of the tilt. We recall that even the LE calculations of Feng *et al.* (2001) showed an unexplained symmetry-breaking process intrinsic in the evolution of the system, i.e., the location of the roll cell that first splits.

As shown in Figs. 4(a)–4(b), this secondary flow, which initially involves only the regions near the side edges, quickly propagates throughout the cross section so that the roll-cell structure soon covers the entire domain.

The appearance and propagation of the flow roll structure is accompanied by the development of corresponding nonuniformities in the local degree of ordering. As shown
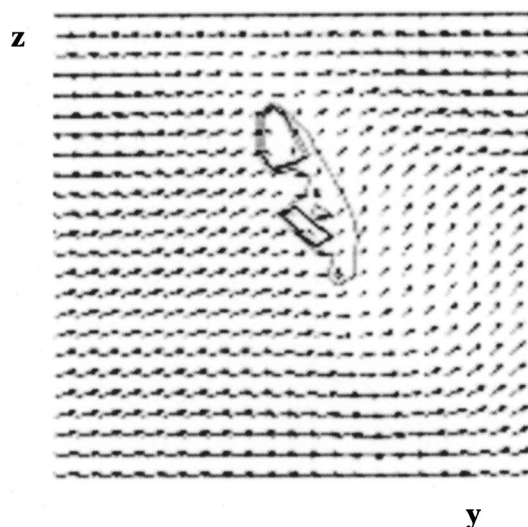
**FIG. 5.** Close-up of the upper right corner [the area is for $y = (7.25-8)$ and $z = (0.25-1)$] of the director vector field with superimposed order parameter contour lines for De $= 20$, $t = 2$ su.

in Fig. 4(c), one can see that the order parameter drops at the roll boundaries (note the dark regions of small order parameter). These nonuniformities in the local degree of order increase in time as can be seen from the evolution of the order parameter fields shown in Fig. 4(d). One can see, that the decrease in the order parameter has become so strong that, in the region between rolls, the configuration tensor is practically isotropic. Although these regions are not line disclinations, they would appear as darkened stripes aligned in the flow direction when viewed between cross polarizers as in the typical optical experiments of Larson and Mead (1993) or Tan and Berry (2003), and it is possible that it is these nonlocalized structures that have been identified as the "disclinations" that form in the region between roll cells.

The roll-cell structure gives rise also to modulations in the orientation field, in which the director tips away from the vorticity direction, along which it was initially oriented, by approximately $20°–30°$, as indicated by the light regions in Fig. 4(e). The degree by which the orientation tips away from the vorticity direction also increases with time as shown in Fig. 4(f). It is important to note, however, that the plots of the director angles taken alone can be misleading, since, in our molecular model, the orientation of the director gives no indication of whether the orientation distribution is nearly isotropic or strongly aligned. For example, the strong gradients of $\phi$ in the upper right corner do not represent any important physics since they appear in a region where the configuration tensor is nearly isotropic. In Fig. 5, we therefore plotted the order parameter superimposed on the director field near the upper right corner of the flow cell during the roll-cell evolution process to highlight the appearance, as described earlier, of strong gradients in the orientation field on the roll-cell boundary. In the region enclosed by the dark contour line, the material is nearly isotropic, while outside of it the orientation smoothly varies. Again, we note that these regions would appear as dark stripes aligned in the flow direction if the sample were observed through crossed polarizers.
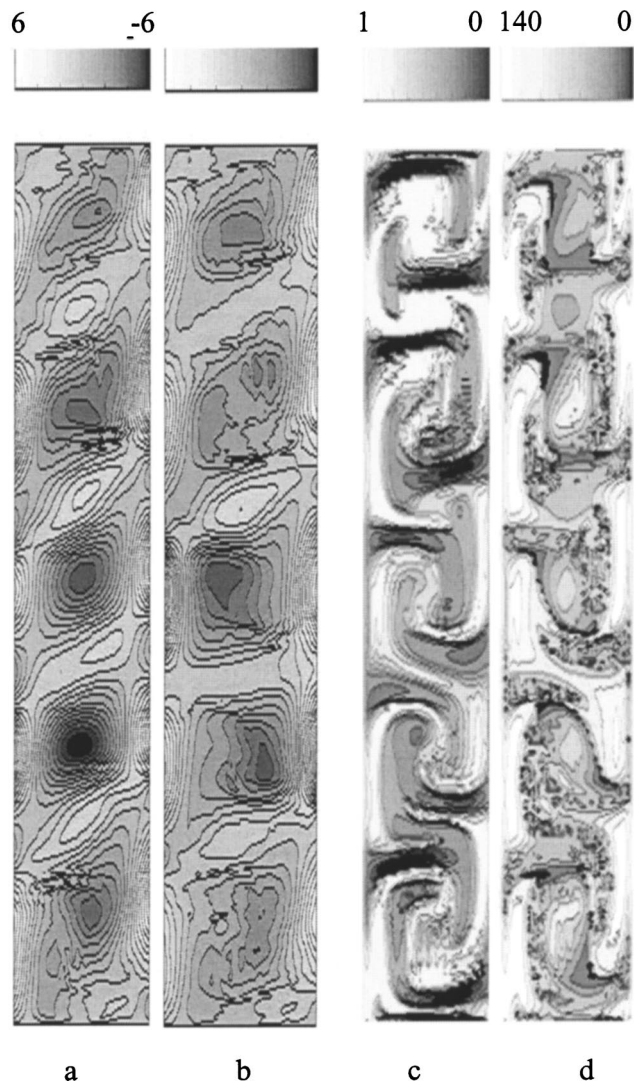
**FIG. 6.** The splitting and breakup of the roll cells for De = 20. (a) The secondary vorticoty $\omega_x$ at $t$ = 2.8 su; (b) the secondary vorticity at $t$ = 3 su; (c) the scalar order parameter at $t$ = 3 su; and (d) the director orientation angle $\phi$ at $t$ = 3 su.

## B. Roll-cell splitting

After covering the entire cross section, the roll-cell structure becomes unstable to violent readjustments of the secondary flow field that results in cell breakup. As we show in Fig. 6, one can observe that some of the original cells progressively split into two areas of recirculation [in Fig. 6(a) only the first roll from the left has started to split, while in Fig. 6(b) both the first and fourth rolls are divided]. These breakup events of the secondary flow rolls are mirrored in the evolution of the microstructure [Figs. 6(c)–6(d). In particular, we see in Fig. 6(d) that sharp gradients in the orientation appear at the center of the original rolls. In Fig. 7 we highlight the two regions of contrasting orientation that are created by the breakup process in one of the splitting rolls. In Fig. 8, we show the same area of Fig. 7 at a slightly later time. At the center of the roll, where the sharp
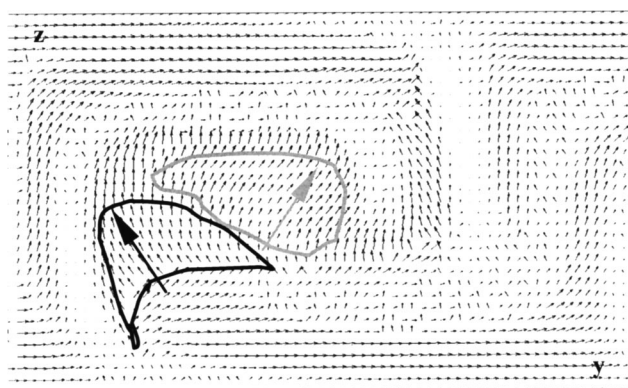
**FIG. 7.** Close-up on the splitting of the first roll from the left: director field at $t = 3.0$ su for De $= 20$; the area shown is $y = (0,2)$ and $z = (0,1)$.

gradients in the orientation had appeared during the roll breakup process, there are now two small regions where the director has escaped away from the vorticity direction and into the flow direction. These regions can be observed near the center of the original roll as a pair of light and dark spots in Fig. 8(a). In Fig. 8(c) we show the corresponding director field and we can notice that the escape of the director toward the flow direction has "resolved" the strong elastic distortions that were present in Fig. 7. It is important to note that these regions are not characterized by a zero value of the order parameter. In other words, they are a pair of defects of the thick type, i.e., without an isotropic core. Other regions of Fig. 8, in which it appears that the orientation has also escaped into the flow direction are fundamentally different since the system is nearly isotropic in the same neighborhood.

This process of cell breakup and generation of thick disclinations mirrors the mechanism that was discovered in the LE calculations by Feng *et al.* (2001), and that was there referred to as the appearance and splitting of "ridges." We will adopt here the same name to describe the process shown in Figs. 6–8, since it appropriately describes the appearance of sharp gradients in the orientation angle and the escaping of the director toward the flow direction.

## C. Long-time gridding and complex patterns

The refinement of the texture, that starts with the breakup events, then continues with the appearance of modulations in the orientation field that are periodic in the shear gradient direction. The straight roll structure with nearly vertical defect lines of Fig. 4, becomes progressively distorted because of the rolls breakup. The nearly isotropic regions become twirls, then we observe a progressive deformation of these patterns leading to stripes layered along the gradient direction. We will call this process "gridding" as it progressively obscures the original (vertical) roll structure with superimposed (horizontal) patterns.

As time progresses, even more complex spatial textures with finer patterns appear. As far as the orientation is concerned, we see that, at these late times the director is mainly in the plane of shear, while it is oriented along the vorticity direction only in a thin region near the anchoring surface.
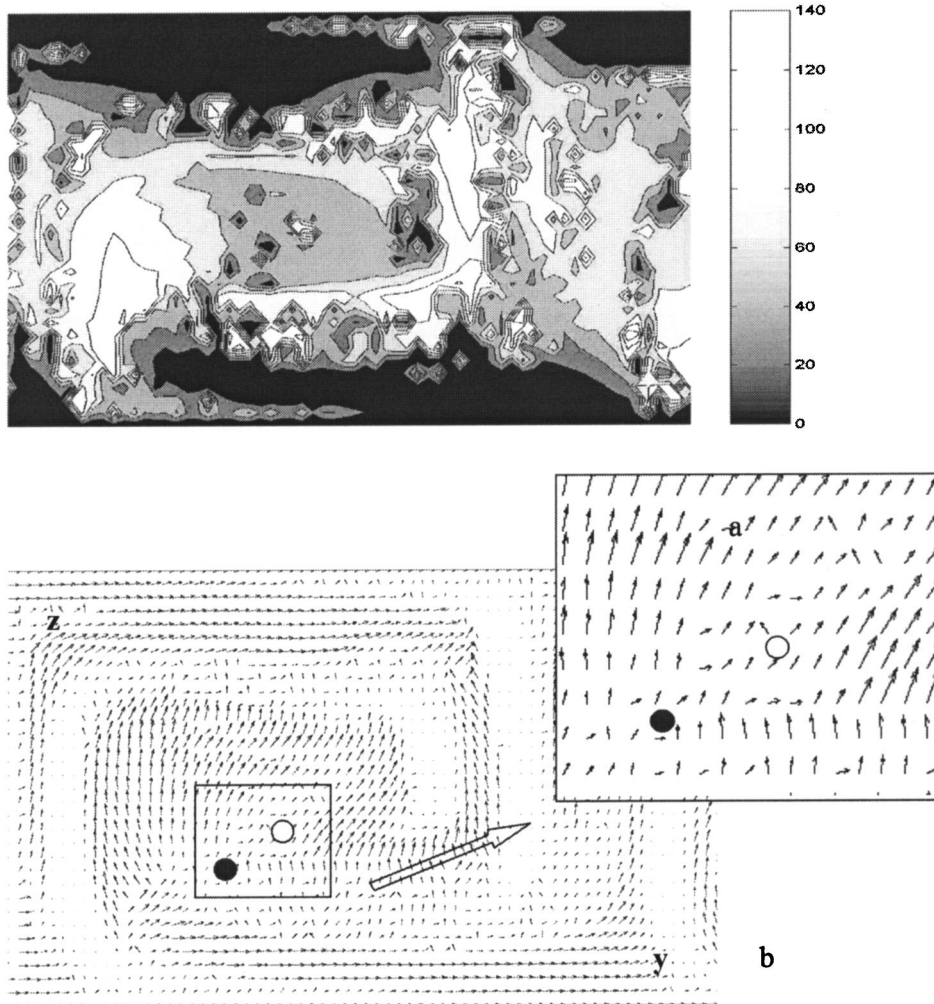
**FIG. 8.** Close-up on the splitting of the first roll from the left at $t = 3.6$ su for De $= 20$. (a) Director angle; (b) prolate director field [the area shown are $y = (0,2)$ and $z = (0,1)$]. with a close-up on the central region [$y = (0.75,1)$ and $z = (0.25,0.5)$].

## D. Macroscopic observables

In Figs. 9–10, we show how the spatial nonhomogeneities in the order parameter and director orientation, the evolution of which we have just described, affect quantities that can be observed in macroscopic experiments.

Specifically in Fig. 9 we show the evolution of the transmitted light intensity (TLI) profiles, the computation of which (from the orientation fields) is described in detail in the thesis by Sgalari (2002). We can see that a well-defined striped pattern appears in the TLI profile just after the appearance of a roll. The characteristic length scale of this pattern, as determined from the analysis of the Fourier spectra of the intensity profile along the $y$ axis, is, initially, of order 1, confirming the direct correlation between the texture observed at the macroscopic level and the flow roll cells (which we remind had a characteristic width of order 1). The texture scale of the TLI then progressively decreases (i.e., the peaks in the Fourier spectrum progressively shift to the left), as a result of the

**FIG. 9.** Evolution of transmitted light intensity profiles in the time interval 2–3 su for De = 2: (a) $t$ = 2.0 su; (b) $t$ = 2.4 su; (c) $t$ = 2.8 su; and (d) $t$ = 3.0 su.

finer structures that appear in the orientation field. This process is sometimes known [Larson and Mead (1992), e.g.] as progressive "phase grating."

In Fig. 10, we plot the evolution of the average birefringence, defined here as the average of $S_{zz} - S_{xx}$ (i.e., opposite in sign to the common definition) over the entire domain. The average value of the birefringence, after an initial transient that reflects the roll-cell formation and breakup, oscillates around very small negative values, indicative of a material partially a ligned in the flow direction with a poor degree of ordering due to the very fine texture. In Fig. 10, we also show the evolution of the rheological response, by plotting the total value of the shear stress and of the first normal stress differences on the upper wall together with the evolution of the average birefringence. One clear correlation between the rheological and optical responses is the contemporary change of sign of the average birefringence and of the first normal stress difference. It is well known, in fact, that the sign of $N_1$ is one of the most clear indicators of the tumbling, wagging or flow-aligning behavior of liquid crystals [Doi and Edwards, (1988), e.g.]. It is also important to note that the first maximum in the magnitude of the wall stress occurs just after the first cell splitting event.

The last plot shown for the case with a Deborah number of 20, is Fig. 11, where we plot the history of the order parameter, of the secondary velocity and of the tumbling angle $\theta$ for a generic point inside the domain [the "random" point chosen is $(4H, 0.25H)$]. The knowledge of the time histories of the orientation and velocity at every point in the domain is, in fact, at the basis of the interpretation for the onset of the instability and the evolution of the texture that we propose in a following section.
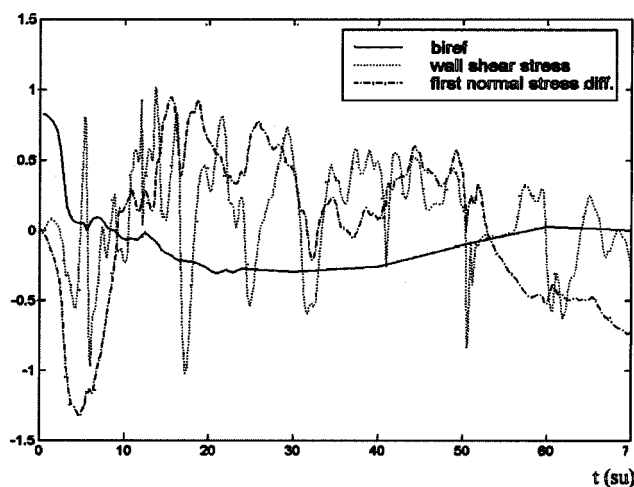


**FIG. 10.** Time evolution of wall stresses and of the average birefringence for De = 20.
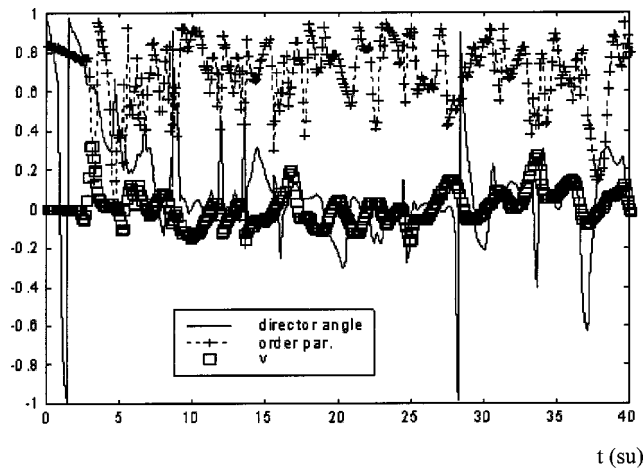
**FIG. 11.** History of the $y$ component of the velocity, of the scalar order parameter and of the director angle $\theta$ (in rad) at the point (4,0.25) for De $=$ 20.

## E. Texture evolution as a function of De number

As previously mentioned, the appearance of secondary flow roll cells is an event common to all values of the De numbers that we considered. Quantitative differences in the roll cell instability with the Deborah number do, however, exist. In particular, the strain at which one observes the onset of the first well-defined roll is strongly dependent on the Deborah number, increasing with increasing De. Figures 3, 12, and 15 show the instant at which the first clearly defined roll structure is observed for the cases De $=$ 20, De $=$ 5, De $=$ 100, respectively. The increase of the onset strain with the Deborah number is less than linear so that the actual onset time (i.e., onset strain/De) decreases with the Deborah number as observed in experiments [at least at low values of the Ericksen number according to Larson and Mead (1992)].

As far as the spatial structure of the rolls is concerned, we see that only the tilt angle of the rolls varies significantly with the Deborah number.
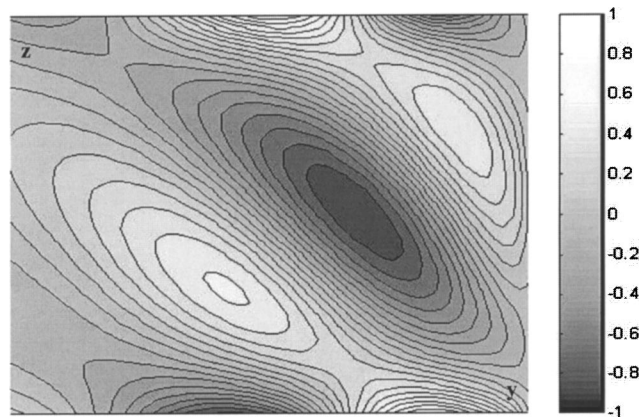


**FIG. 12.** Secondary vorticity field $\omega_x$ near the right side of the flow cell; De $=$ 5, $t$ $=$ 1 su: The area shown is for $y$ (6–8) and $z$ (0–1).
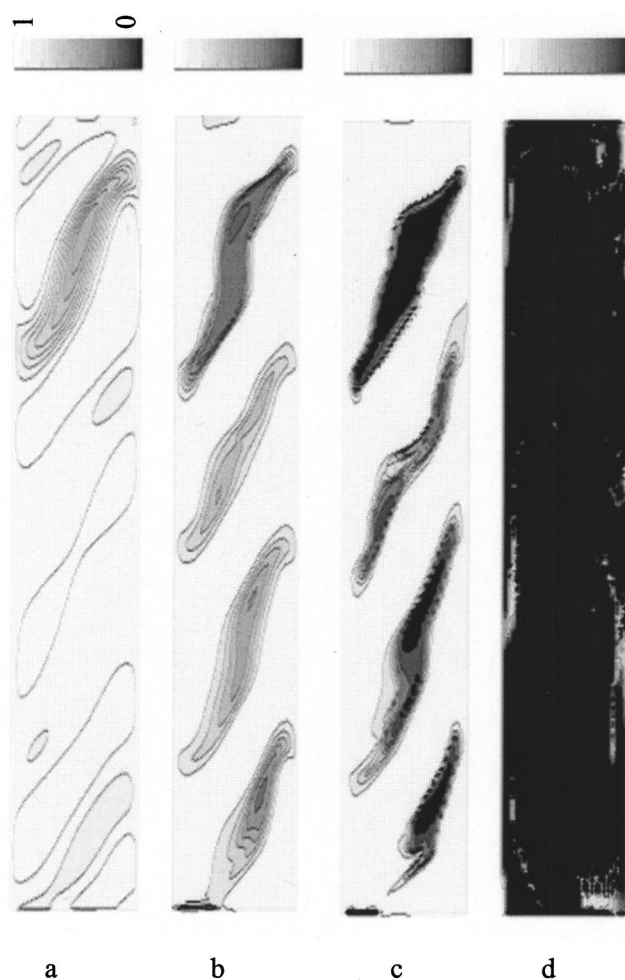
**FIG. 13.** (a) Order parameter field at $t = 0.8$ su; (b) order parameter field at $t = 1.2$ su; (c) order parameter field at $t = 1.6$ su; and (d) order parameter field at $t = 3.6$ su for De $= 5$.

The evolution of the system after the initial formation of rolls can be qualitatively different depending on the value of De considered.

In particular, for the lower value of the De number considered, 5, i.e., a value for which the system is predicted to be in the tumbling regime, the appearance and propagation of the roll cells is followed by a more violent process of cell breakup. Correspondingly, as it is shown in Figs. 13(a)–13(d), the local degree of order monotonically decreases throughout the sample, until the cell appears to be filled by a completely isotropic material. The evolution of the average birefringence clearly reflects this process. As shown in Fig. 14, it quickly decreases to negligible values.

We can interpret these results by realizing that for the case of De $= 5$, the system is naturally driven to a state where the nonuniformities in the orientation field involve molecular length scales. Due to the finite mesh size we use in our computations, our spatial discretization is not able to capture the completion of the refinement process and, instead, shows the misleading picture of a fully isotropic material. As we will discuss in more detail in the following section, when the nonuniformities that develop in our system
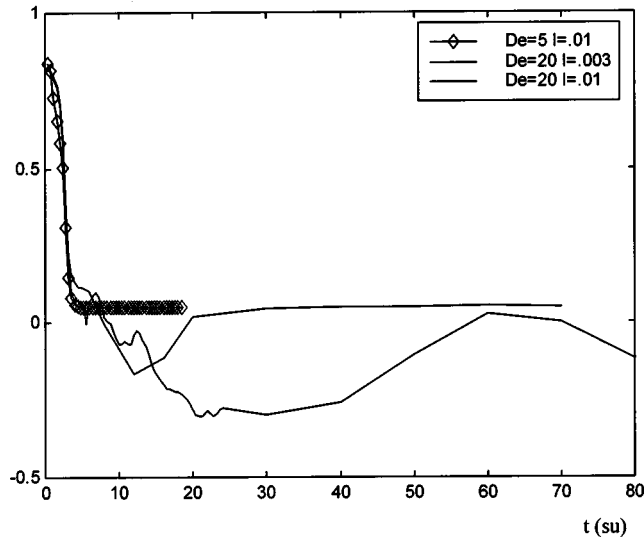
**FIG. 14.** Evolution of the average birefringence for De = 5 and De = 20, $\lambda/H = 0.001$ and $\lambda/H = 0.03$.

become comparable to the mesh size, the averaging process intrinsic in the coarse-grain computation becomes inappropriate. We believe, in fact, that only a statistical treatment of the type used in the analysis of conventional turbulence could hope to achieve the spatial resolution needed to capture the final state of extremely fine worm texture that characterizes systems in the tumbling regime.

For the higher De number, i.e., De = 100, the evolution of the secondary flow field is similar to that discussed for De = 20. The main quantitative difference is the longer periods of oscillation for the macroscopic quantities such as birefringence and wall stresses. The evolution of the configuration field for these high shear rates is also similar to that already described with complex spatial patterns of nonuniform order and orientation alternating in time. The main qualitative differences that we detected between these patterns and those observed for De = 20 is that the characteristic magnitude of the nonhomogeneities is smaller (the magnitudes of the secondary vorticity are $\sim 1/4$ of those observed for the case De = 20 as shown in Fig. 15), that the roll-cell pattern appears slightly more regular and most of all they maintain their good definition much longer in time. It is, however, impossible to quantify these observations with a comparison of well-defined length scales, due to the irregularity of all spatial fields. The only
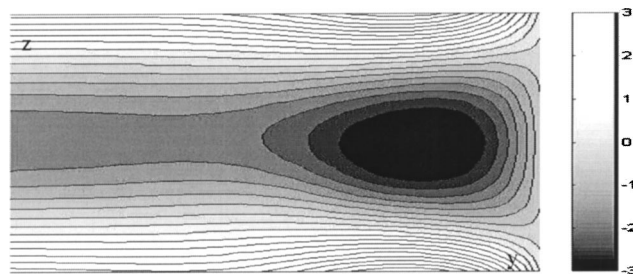


**FIG. 15.** The secondary vorticity $\omega_x$ near the right side of the flow cell at $t = 2.4$ su for De = 100 [the area shown is $y = (6,8)$ and $z = (0,1)$].
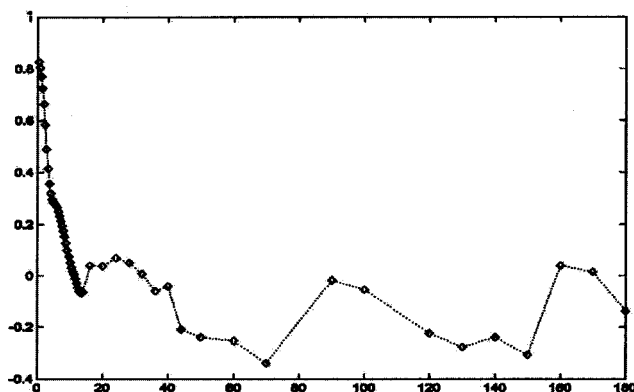
**FIG. 16.** Time evolution of the average birefringence for De = 100.

observation is that the characteristic length scales, which can be obtained by a Fourier analysis of the TLI profiles, are not significantly different than the corresponding length scales for the well-defined structures of Fig. 4.

Related to the longer persistence of these well-defined structures, we see in Fig. 16 that, after an initial transient, the average birefringence slowly oscillates around a value of −0.2, indicative of a material which performs slow wagging motion around the flow direction as is expected for this high value of shear rate (we remind the reader that the Bingham closure cannot predict a transition to flow-aligning behavior even at very high shear rates, but instead predicts a wagging motion with decreasing magnitude as the shear rate is increased).

We believe that the difference in the time histories of the director tumbling angle between the cases De = 20 and De = 100 (Figs. 11 and 17) can also explain the qualitative differences in the long time textures. We see that the two cases show very different behavior in the evolution of the orientation, i.e., tumbling versus wagging. We can note,
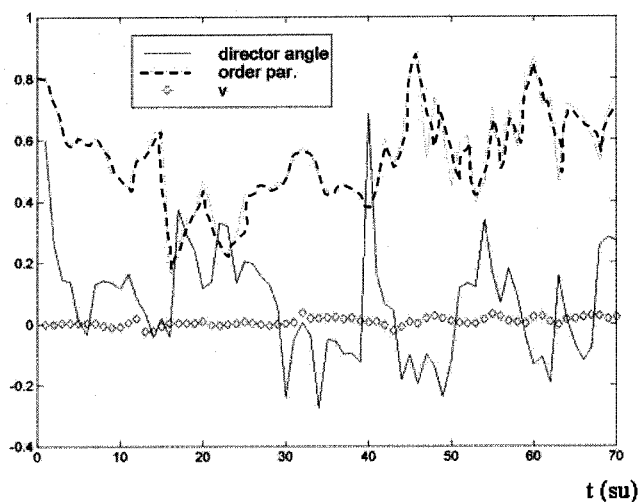


**FIG. 17.** History of the $y$ component of the velocity, of the scalar order parameter and of the director angle $\theta$ (in rad) at the point (4−0.25) for De = 100.
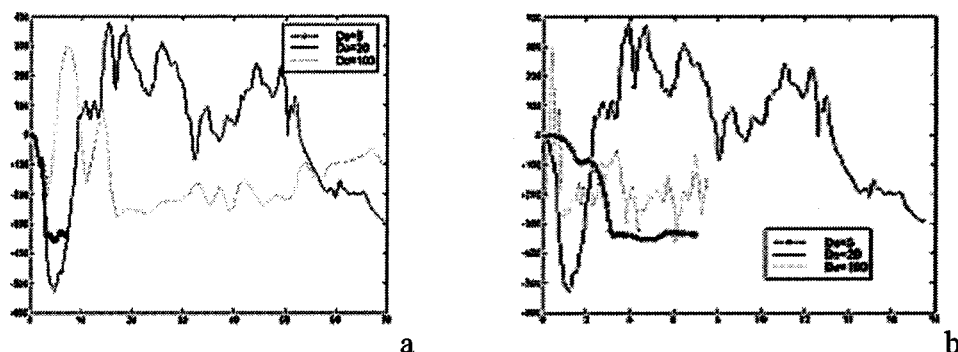
**FIG. 18.** Comparison of the transients of the wall first normal stress difference. for De = 5, De = 20, and De = 100. (a) Evolution with strain; (b) evolution with actual time.

as already mentioned, that the amplitudes of oscillating secondary velocity and order parameter strongly decrease for the case of De = 100 (i.e., for a system in the wagging regime). This observation supports the qualitative picture that we will present in the next section on the intimate relation between tumbling, defect appearance and texture evolution.

The earlier-described differences in the evolution of the orientation with the De number are mirrored in differences in the macroscopic rheological responses shown in Fig. 18. For the case of De = 5, the stress soon plateaus due to the fact that the system, at the mesoscopic level, has been driven to an isotropic state. The oscillations instead persist for the cases De = 20 and De = 100, with the oscillations for De = 20 of a higher magnitude. We also observe that the first normal stress differences do not scale with strain (i.e., the rheological responses coincide only at very early times, before the completion of the roll-cell instability). As already noted for the onset time of roll cells, the initial evolution of roll cells after formation is in fact characterized by a time scale that is in between strain and actual time.

## F. Texture evolution as a function of Er number

As mentioned in Sec. III D we tested a case with larger values of Er number (i.e., smaller $\lambda/H$: 0.001) to understand how the evolution of texture varies with the strength of distortional elasticity.

We see that the areas between roll cells where the order parameter is strongly reduced are much larger (Fig. 19) and the average value of the birefringence oscillates around values much closer to zero (Fig. 14). Moreover, after an initial transient, that is similar to that for larger $\lambda/H$, the wall stress plateaus (Fig. 20). Due to the fact that the system has become very poorly ordered, the orientational stress contribution becomes, in fact, negligible.

To understand the origin of these qualitative differences in the evolution of optical and rheological properties, we plotted in Fig. 21 the time history of the director tumbling angle. We note that for this smaller value of $\lambda/H$, the tumbling oscillations persist at all times unlike in the case for $\lambda/H = 0.03$. In other words, due to the low strength of distortional elasticity, local oscillations are not dampened out.

**FIG. 19.** (a) The scalar order parameter field at $t = 2$ su for $\lambda/H = 0.03$; (b) the scalar order parameter field at $t = 2$ su for $\lambda/H = 0.001$.

## V. DISCUSSION

Our simulations showed that the theoretical model and computational procedures are capable of capturing, at least at a qualitative level, the flow instability and the ensuing striped texture that are the distinctive features of the textural evolution of actual sheared LCPs.

In particular, our simulations confirm the physical connection between tumbling behavior and the striped texture. Application of a shear rate below the flow-alignment
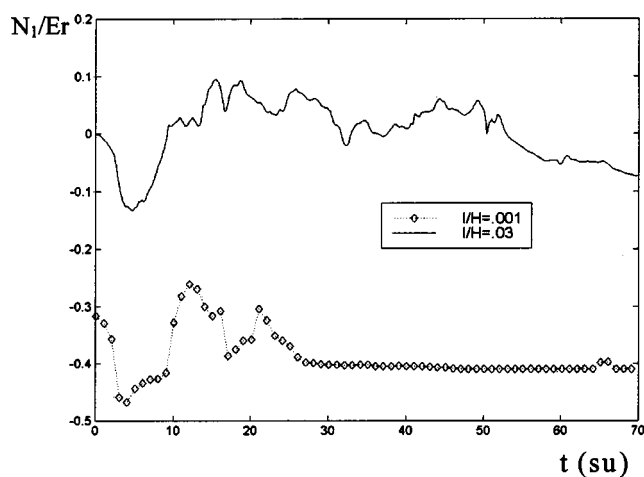
**FIG. 20.** Evolution of the wall first normal stress difference divided by the Er number for $\lambda/H = 0.001$ and $\lambda/H = 0.03$, and De $= 20$.

transition causes massive director tumbling after strains of order unity. The competition between the periodic fluctuations in orientation, which would result from free tumbling, and the anchoring conditions on the boundaries results in high elastic stresses with periodic flow modulations and defect generation at the boundaries of the rolls of secondary flow (Fig. 5).

The absolute value of the strain at which one observes the appearance of the striped pattern in our simulations ranges from 1 to 3 su depending on the value of De number, and is slightly smaller than that observed in experiments for the PBG solutions of the Larson and Mead experiments with vorticity anchoring (i.e., $\sim 20$ su) and more similar to that observed for the same systems when the anchoring of the orientation was in the flow direction (i.e., $< 5$ su). We believe that the difference is partially due to the fact that, in the experiments, the boundary and initial conditions are not perfectly uniform. Differences in the type of anchoring would lead to significant differences in the time scales of the evolution. Much better agreement is obtained, for example, with the experiments on PBT solutions with vorticity anchoring [Srinivasarao and Berry (1991)]. In these systems a texture started to appear after only a fraction of strain unit had been applied. It is important to remember, however, that any discussion on the absolute magnitude of the predicted onset strain has to be taken with caution. As simulations with the finer mesh indicate, the effect of numerical truncation errors in the definition of spatial gradients is effectively accelerating the instability thus reducing the time for the readjustments of orientation and the onset of the instability itself.

Some of the features of this instability are similar to what has been observed in experiments at low values of the Ericksen number [Larson and Mead (1992)], and is in partial agreement with simplified predictions done in the context of the Leslie-Ericksen theory (Feng *et al.* (2001)]. In particular, we found that the aspect ratio of the rolls and the onset time for the appearance of texture vary with the shear rate (as indicated in the previous section) in a fashion that is similar to the one reported in the work by Larson and Mead (1992) for a material in the Ericksen number cascade. We believe that this is due to the particular initial condition we have chosen, i.e., a equilibrium uniaxial monodomain, that allows us to probe, at start-up, the mechanism of pure roll-cell onset.
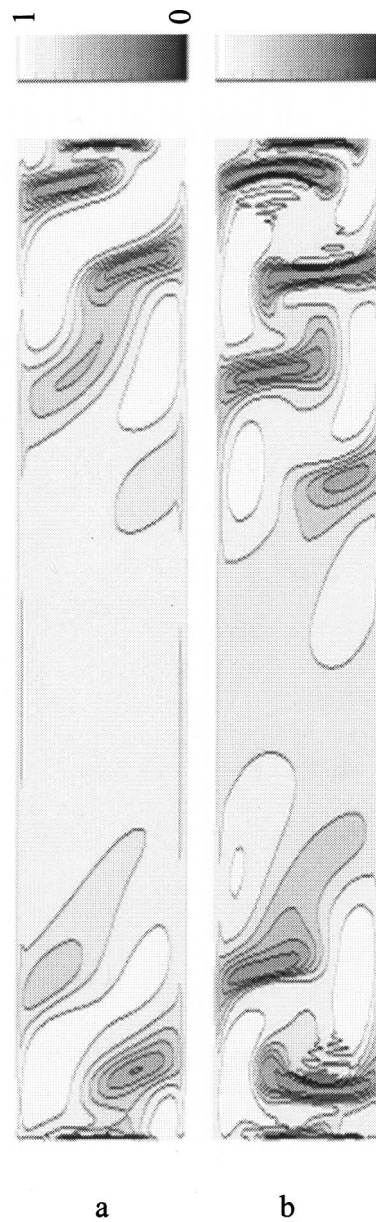
**FIG. 21.** (a) The scalar order parameter field at $t = 2$ su for $\lambda/H = 0.03$; (b) the scalar order parameter field at $t = 2$ su for $\lambda/H = 0.001$.

As time progresses, the orientation becomes, on average, progressively distorted from the equilibrium uniaxial orientation. Specifically, after a couple of strain units, strong nonuniformities in the order parameter appear. These regions in which the degree of order becomes negligible are, we believe, thin disclinations between roll cells. This aspect of texture evolution is missing in the LE description of the roll-cell structure and, as stated in the introduction, is one of the essential features of the evolution of texture in real liquid crystalline polymers at higher shear rates.

Our simulations moreover also retained the mechanism that was observed in the LE simulations with the nucleation of thick defects at the center of rolls. In particular, we were able to predict breakup (or cell splitting) events of the original roll cells and the formation of thick disclinations that, at least from a qualitative point of view, do not differ from those predicted in the work of Feng *et al.* (2001).

A detailed comparison between the predictions of our calculations and the work by Feng *et al.* is, however, not possible. The fact that the system is, in general, characterized by strong distortions of the orientation distribution is indeed proof that molecular effects are very important and cannot be neglected, as instead was done in the LE calculations. For the overall evolution of the system, we will make therefore a comparison only with experimental observations. The only macroscopic quantities for which experimental data are available are the TLI profiles, the average measure of orientation, and rheological measurements of wall normal and shear stresses. For these quantities, the qualitative trends agree with what is observed experimentally.

In particular, we were able to capture the process of progressively refining texture, which is an essential feature of experimental images. Moreover, the fact that this refinement process leads, for the lower value of the De number we analyzed (i.e., a value below the tumbling-wagging transition) to a material that is isotropic at the coarse-grain level of a continuum description is in agreement with the existing observations for LCPs in the tumbling regime [Larson and Mead (1993)]. As already mentioned in the previous section, when real domains reach microscopic sizes, observations at the mesoscopic level have to average over several uncorrelated domains, so that the material appears isotropic.

For larger values of the shear rate, the polydomain structure that develops can dampen out local fluctuations. In fact large-scale oscillations in the orientational field are still observed at late times but they do not strongly affect the average values of the macroscopic optical and rheological observables. In our simulations, these oscillations are largest for shear rates close to the tumbling-wagging transition in agreement with the theoretical prediction of large scale flow instabilities near such a transition [Magda *et al.* (1991)]. This fact can be also related to the experimental observation that the striped textures that appear for shear rates in the wagging regime are much more distinct and persistent than those for lower or higher values of shear rate [Larson and Mead (1993)].

As a note of caution, however, we remind the reader that, even if the sequences of TLI profiles that we have shown in the previous section seem consistent with those observed in real materials, we are not able to make any prediction on the length distribution of the stripes (i.e., the characteristic scale of these pattern along the flow direction), because in our simplified geometry we do not allow variation along the flow direction. Moreover, the TLI profiles do not discriminate between the various orientation patterns across the gap, i.e., the different types of spatial nonuniformities cannot be inferred by TLI images, so that a clear verification of our predictions for the microstructure field is not possible at the present time and experimental images of the local configuration are needed.

Even more delicate is the issue of comparing the evolution of the average orientation with experimental data due to the existing large discrepancies in the available experimental values depending on the method used. These discrepancies lead to sometime contradictory results [for a complete discussion of the issue see Hongladarom *et al.* (1996)], and, according to the same authors, are indicative of intrinsic limitations of the various experimental techniques. Accordingly, some measure of restraint is called for when attaching detailed structural significance to the measured orientation parameters and it is safer to use them only for qualitative comparisons of trends and parameter dependence.

The rheological transients that our simulations predict compare well with optical ones, as observed in experiments (e.g., the strong similarities between stress transients and

transients of conservative dichroism in Moldenaers and Mewis (1986)], in that they displayed damped oscillations and evolve on similar strain scales. However, no detailed information on the microstructural origin can be extrapolated from a direct comparison of such data and we believe that only detailed knowledge of the evolution of orientation, like the one provided here for a simplified geometry and for a few relevant cases can provide the correct physical interpretation of any type of rheological and optical data and shed light on the complex interplay between flow and texture that is found in sheared LCP systems.

## VI. CONCLUSIONS

The results shown in the present work indicate that the theoretical model that was previously developed in our group [Feng *et al.* (2001)] is capable of predicting, at least qualitatively, many of the salient features of the textural evolution of sheared LCP materials. Insights into the physical mechanisms that determine the characteristic striped texture are obtained, and the predicted scaling compares well with the limited data available from experimental observations.

Further work to analyze fully three-dimensional geometries is, however, needed to better judge the ability of the theoretical model to accurately describe the behavior of LCPs in shear. In particular, it is still to be determined whether the model can correctly capture, when applied to a 3D geometry, the full sequence of textural transitions, i.e., appearance of birefringent bands, transition to stripes, and progressive refinement of the striped texture.

## ACKNOWLEDGMENT

## References

Chaubal, C. V., and L. G. Leal, "A closure approximation for the liquid crystalline polymer models based on parametric density estimate," J. Rheol. **42**, 177–201 (1998).

Doi, M., and S. F. Edwards, *The Theory of Polymer Dynamics* (Oxford University Press, New York, 1988).

Edwards, B. J., "Evaluation of the thermodynamic consistency of closure approximations in several models proposed for the description of liquid crystalline dynamics," J. Non-Equil. Thermodyn. **27**, 5–24 (2002).

Feng, J., C. V. Chaubal, and L. G. Leal, "Closure approximations for the Doi theory: Which to use in simulating complex flows of liquid crystalline polymers?" J. Rheol. **42**, 1095–1119 (1998).

Feng, J., and L. G. Leal, "Pressure driven channel flows of a model liquid crystalline polymer," Phys. Fluids **11**, 2821–2835 (1999).

Feng, J., G. Sgalari, and L. G. Leal, "A theory for flowing nematic polymers with orientational distortions," J. Rheol. **44**, 1085–1101 (2000).

Feng, J., J. Tao, and L. G. Leal, "Roll cells and disclinations in sheared polymer nematics," J. Fluid Mech. **41**, 1317–1335 (2001).

Gleeson, J. T., R. G. Larson, G. Kiss, and P. E. Cladis, "Image analysis of shear-induced textures in liquid crystalline polymers," Liq. Cryst. **11**, 341–364 (1992).

Hongladarom, K., V. M. Ugaz, D. K. Cinader, W. R. Burghardt, J. P. Quintana, B. S. Hsiao, M. D. Dadmun, W. A. Hamilton, and P. D. Butler, "Birefringence, x-ray scattering and neutron scattering measurements of molecular orientation in sheared liquid crystal polymer solutions," Macromolecules **29**, 5346–5355 (1996).

Kupfermann, R., M. N. Kawaguchi, and M. M. Denn, "Emergence of structure in a model of liquid crystalline polymers with elastic coupling," J. Non-Newtonian Fluid Mech. **91**, 255–271 (2000).

Larson, R. G., "Roll-cell instabilities in shearing flows of nematic polymers," J. Rheol. **37**, 175–196 (1992).

Larson, R. G., and D. W. Mead, "Development of orientation and texture during shearing of liquid crystalline polymers," Liq. Cryst. **12**, 751–768 (1992).

Larson, R. G., and D. W. Mead, "The Ericksen number and the Deborah number cascades in sheared polymeric nematics," Liq. Cryst. **15**, 151–169 (1993).

Lathrop, D. P., J. Fineberg, and H. L. Swinney, "Turbulent flow between concentric cylinders at large Reynolds number," Phys. Rev. Lett. **68**, 1515–1518 (1992).

Lele, S. K., "Compact finite difference schemes with spectral-like resolution," J. Comput. Phys. **103**, 16–42 (1992).

Magda, J. J., S. G. Baek, K. L. de Vries, and R. G. Larson, "Shear flows of liquid crystal polymers: Measurements of the second normal stress difference and the Doi molecular theory," Macromolecules **24**, 4460–4468 (1991).

Manneville, P., "The transition to turbulence in nematic liquid crystals," Mol. Cryst. Liq. Cryst. **70**, 1501–1528 (1981).

Marrucci, G., and F. Greco, "The elastic constants of Maier–Saupe rodlike molecule nematics," Mol. Cryst. Liq. Cryst. **206**, 17–30 (1991).

Marrucci, G., and F. Greco, "Flow behavior of liquid crystalline polymers," Adv. Chem. Phys. **86**, 331–404 (1994).

Mather, P. T., D. Pearson, and R. G. Larson, "Flow patterns and disclination-density measurements in sheared neamtic liquid crystals," Liq. Cryst. **20**, 527–538 (1996).

Moldenaers, P., and J. Mewis, "Transient behavior of LC solution of PBG," J. Rheol. **30**, 567–584 (1986).

Sgalari G., "Rheology and texture of liquid crystalline polymers," PhD thesis, University of California, Santa Barbara, CA, 2002.

Sgalari, G., J. J. Feng, and G. L. Leal, "The shear flow behavior of LCPs based on a generalized Doi model with distortional elasticity," J. Non-Newtonian Fluid Mech. **102**, 361–382 (2002).

Srinivasarao, M., and G. C. Berry, "Rheo-optical studies on aligned nematic solutions of a rodlike polymer," J. Rheol. **35**, 379–397 (1991).

Tan, Z., and G. C. Berry, "Studies on the texture of nematic solutions of rodlike polymers: 3. Rheo-optical and rheological behavior in shear," J. Rheol. **47**, 73–104 (2003).

Vermant, J., P. Moldenaers, S. J. Picken, and J. Mewis, "A comparison between texture and rheological behavior of lyotropic liquid crystalline polymers during flow," J. Non-Newtonian Fluid Mech. **53**, 1–23 (1994).

Walker, L. M., P. Moldenaers, S. J. Picken, and J. Mewis, "The defect texture of LCP solution under shear," Rheol. Acta **39**, 26–37 (2000).

Wang, Q., and E. Weinan, "Kinetic theory for flows of nonhomogenous rodlike liquid crystalline polymers with a nonlocal intermolecular potential," Phys. Rev. E **65**, 051504/1–7 (2002).